Available online at www.sciencedirect.com

ScienceDirect

Journal of Ocean Engineering and Science 1 (2016) 268–283

www.elsevier.com/locate/joes

Prediction of regular wave loads on a fixed offshore oscillating water column-wave energy converter using CFD

Ahmed Elhanafi [a,b,*]

[a] National Centre for Maritime Engineering and Hydrodynamics, Australian Maritime College, University of Tasmania, Launceston, Tasmania 7250, Australia
[b] Department of Naval Architecture and Marine Engineering, Alexandria University, Alexandria, Egypt

Received 24 June 2016; received in revised form 29 July 2016; accepted 2 August 2016
Available online 23 September 2016

Abstract

In this paper, hydrodynamic wave loads on an offshore stationary–floating oscillating water column (OWC) are investigated via a 2D and 3D computational fluid dynamics (CFD) modeling based on the RANS equations and the VOF surface capturing scheme. The CFD model is validated against previous experiments for nonlinear regular wave interactions with a surface-piercing stationary barge. Following the validation stage, the numerical model is modified to consider the pneumatic damping effect, and an extensive campaign of numerical tests is carried out to study the wave–OWC interactions for different wave periods, wave heights and pneumatic damping factors. It is found that the horizontal wave force is usually larger than the vertical one. Also, there a direct relationship between the pneumatic and hydrodynamic vertical forces with a maximum vertical force almost at the device natural frequency, whereas the pneumatic damping has a little effect on the horizontal force. Additionally, simulating the turbine damping with an orifice plate induces higher vertical loads than utilizing a slot opening. Furthermore, 3D modeling significantly escalates and declines the predicted hydrodynamic vertical and horizontal wave loads, respectively.

Keywords: Offshore oscillating water column; OWC; Hydrodynamic wave loads; Numerical wave tank; CFD; 3D effects.

1. Introduction

Nowadays, wave energy is one of the greatest future renewable energy resources, and research is being conducted worldwide. Oscillating water column (OWC) is a wave energy extraction device that uses the incoming ocean wave' oscillations to drive an oscillating column in a pneumatic chamber that has an opening to the sea. As the water level inside the OWC chamber moves up and down, it compresses and decompresses the air, respectively. Air energy is then converted into mechanical energy by means of a bi-directional air turbine connected to the pneumatic chamber. Electricity can then be generated by utilizing an electric generator that converts the mechanical energy to useful electricity. For its simplicity from operation point of view and having no moving parts underwater that provides lesser and easier maintenance works, OWC has drawn attention of many researchers as one of the most promising wave energy converters.

A theoretical model of the hydrodynamics for a fixed OWC device was developed by Evans [1] who ignored the spatial variation and assumed a rigid weightless piston motion for the chamber's internal free surface of a small width relative to the incident wavelength. These assumptions allowed the application of the oscillating body theory. The rigid-body approach was then improved by Falcão and Sarmento [2], Evans [3] and Falnes and McIver [4] by allowing the increase in pressure at the free surface as well as providing the possibility of a non-plane free surface. To validate the oscillating surface pressure theory proposed by Sarmento and Falcão [5] in OWCs, Sarmento [6] carried out a set of wave flume experiments utilizing very small steepness regular waves with linear and quadratic power take-off (PTO) represented by filters and orifice plate, accordingly. Morris-Thomas et al. [7] and Ning

* Correspondence to: National Centre for Maritime Engineering and Hydrodynamics, Australian Maritime College, University of Tasmania, Launceston, Tasmania 7250, Australia.
E-mail address: Ahmed.Elhanafi@utas.edu.au.

http://dx.doi.org/10.1016/j.joes.2016.08.001

et al. [8] experimentally investigated the impacts the underwater chamber's geometry has on onshore OWCs performance.

Adding to the analytical and experimental studies, Numerical Wave Tank (NWT) based on potential flow solver or solving the Reynolds–averaged Navier–Stokes (RANS) equations are also being used. In contrast to potential flow models, RANS models do not have the shortcomings of handling problems with strong nonlinearity, dispersion, wave breaking, complex viscous, turbulence and vortex shedding. On the other hand, with potential flow solvers, the solution can be obtained in a reasonable time on standard computers. Usually, potential flow models are solved using Boundary Element Method (BEM). Studies on OWCs that implement potential flow solvers are for instance, Brito-Melo et al. [9], Delauré and Lewis [10], Josset and Clément [11], Lopes et al. [12], Sykes et al. [13, 14] and Gomes et al. [15].

With increasing the computation power, RANS models became more attractive for researchers to study the OWC hydrodynamic performance. Examples that implemented CFD models for investigating the impacts the environmental conditions (wave height and period), the chamber underwater geometry and PTO damping have on the hydrodynamic performance of onshore OWC devices include Zhang et al. [16], Teixeira et al. [17], López et al. [18], Kamath et al. [19, 20], Luo et al. [21], Anbarsooz et al. [22], Şentürk and Özdamar [23] and Elhanafi et al. [24].

In contrast to onshore OWCs, offshore OWCs do not have the chamber rear wall extending to the seabed. As a result, offshore OWCs allow the ocean waves to pass around and underneath the device walls. Recently, Iturrioz et al. [25, 26] developed and validated a CFD model based on RANS–VOF using open source code (IHFOAM) with tank flume experiments to study the hydrodynamics and pneumatics of a fixed detached OWC. Crema et al. [27] studied experimentally the efficiency of an OWC designed for installation on a floating structure. The study included different geometrical parameters and both regular and irregular waves under different pneumatic damping. Simonetti et al. [28] presented the numerical settings of an open source CFD code (OpenFOAM) and validation results against physical measurements of a similar OWC device tested by Crema et al. [27]. Elhanafi et al. [29] utilized a 2D validated numerical model based on (RANS–VOF) using a commercial CFD code (Star–CCM+) with experimental results to uncover the impact of increasing the incident wave amplitude, frequency and turbine damping on the energy balance of an offshore stationary-floating OWC through detailed energy balance analyses. Using a 2D CFD model, Elhanafi et al. [30] studied the impact of the underwater chamber' lips thickness and submergence on the hydrodynamic performance of an offshore OWC under a constant wave height and PTO damping. They observed that with increasing the asymmetric lips submergence ratio (rear wall draught to front wall draught), the rear wall thickness or an appropriate combination between the asymmetric lips submergence and thickness, the overall hydrodynamic efficiency can considerably be escalated over a broad frequency bandwidth.

Providing a better understanding of the offshore OWCs hydrodynamic performance is important; however studying the hydrodynamic loads on these devices is essential for their stability and continuation in operation safely. There is a limited research focusing on studying these loads such as Jayakumar [31] who experimentally found that the wave forces on OWC caisson breakwater when air damping inside the OWC model is less were smaller than the traditional rectangular caisson. Ashlin et al. [32] experimentally quantified the horizontal and vertical wave forces on an onshore OWC model scale with constant pneumatic damping in a 2D wave flume. They studied, the effect of wave steepness and relative water depth on the measured wave forces, and observed that at natural frequency of system, the force on the structure is less.

The present paper aims to develop and validate a CFD model based on RANS equations solver with a VOF surface capturing scheme introduced by Hirt and Nichols [33] (RANS–VOF) to preliminary investigate the hydrodynamic wave loads acting on an offshore OWC model scale. The study includes a validation against existing experiments and then discovering the relevance of the incoming wave period, wave height, PTO damping, PTO and 3D modeling to the horizontal and vertical wave forces and their nonlinearity.

2. Numerical wave tank (NWT)

2.1. Governing equations

The Computational Fluid Dynamics (CFD) model utilized in the present study is a fully nonlinear model that is based on the RANS equations together with VOF surface capturing scheme introduced by Hirt and Nichols [33]. For the small OWC model scale considered in this investigation, air compressibility inside the OWC chamber has a negligible effect. Accordingly, the NWT used in the present study assumes incompressible flow, and the continuity and RANS equations are used to describe the flow motion via using a commercial CFD code (Star–CCM+). In order to mathematically close the flow sets of equations, the two-equation Shear Stress Transport (SST) k—ω turbulence model is implemented to model the Reynolds Stresses in RANS equations.

2.2. Computational fluid domain

In this section, only settings for 2D CFD model is presented. A 10 wavelengths (L) NWT with 2 cells in width is used in the present study with boundary conditions defined as in Fig. 1a. To reduce the unwanted reflected waves from the NWT downstream outlet boundary, one wavelength at the end of the fluid domain is assigned for damping the transmitted waves underneath the structure. The hydrodynamic wave interaction with a bluff body such as an OWC will produce a partial standing wave envelope in front of the OWC structure; therefore, a sufficient refined free surface zone of three times the incoming wave height (H) is used. Considering that ocean waves are the main exciting source acting on offshore structures like OWCs, proper modeling of these waves is

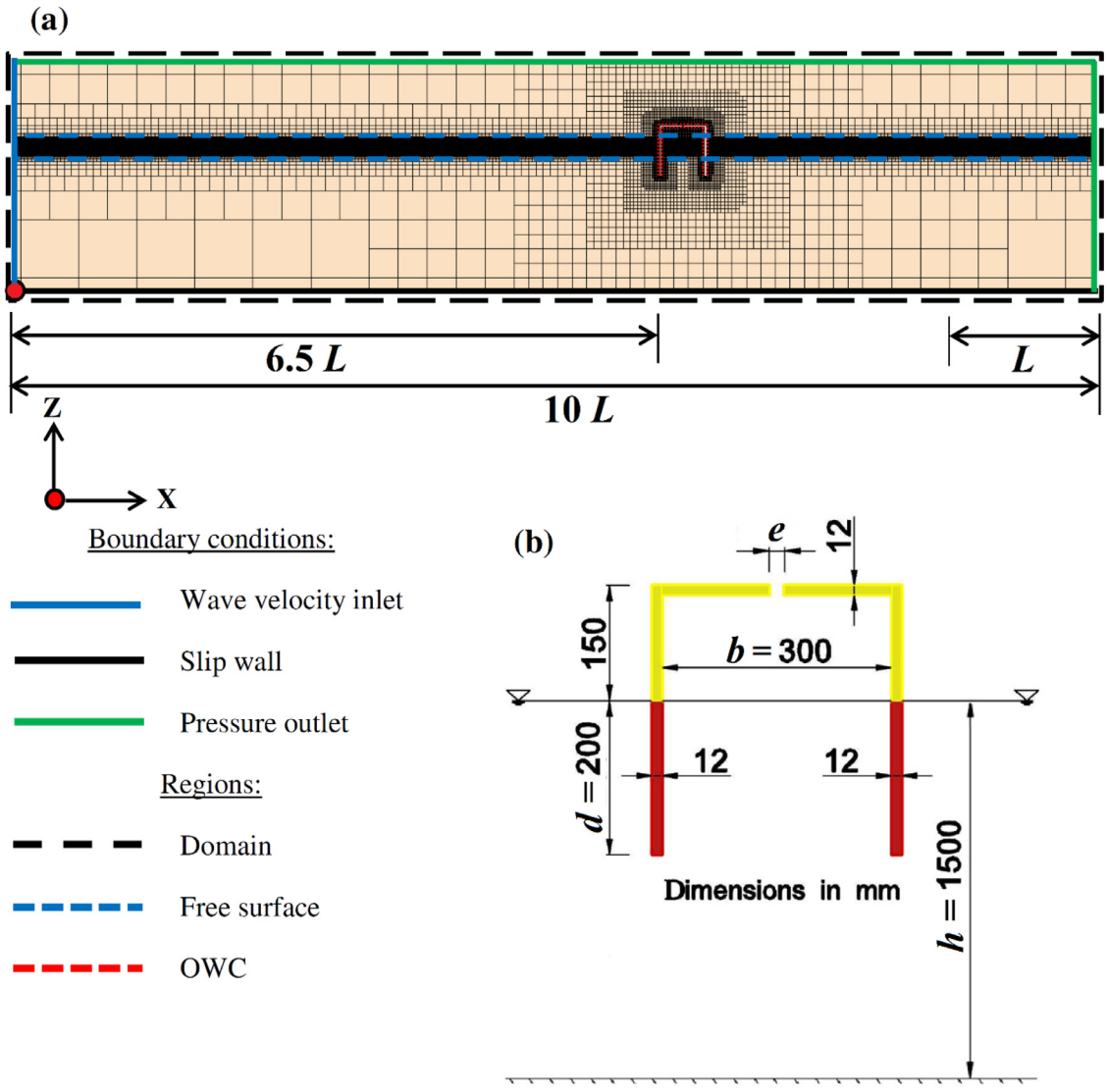

Fig. 1. (a) Computational fluid domain and (b) offshore OWC 1:50 model scale.

paramount for accurate prediction of the hydrodynamic loads, structure's response and performance [34]. Accordingly, the gird and time step recommended by Elhanafi et al. [24] are implemented in the present study. Elhanafi et al. [24] found that a domain base cell size of 400 mm with free surface grid size of at least 12 and 36 cells per wave height and wavelength while maintaining a maximum cell aspect ratio of 16 are recommended for accurately generate waves with less than 1.0% deviation from the analytical input wave height when using a second-order temporal discretization scheme with 1200 time steps per wave period (T).

A mesh convergence study was performed considering five different surface mesh sizes for the OWC' walls (Fig. 1b) under a wave height of H=50 mm, wave period T=1.2 s and PTO slot opening of e=5.0 mm. The cell surface size of the coarser mesh (Mesh1) was 25 mm, and the total cells count 170,000. More refinement was applied with 12.5 mm (Mesh2), 6.25 mm (Mesh3), 3.125 mm (Mesh4) and the most refine mesh of 1.5625 mm (Mesh5) surface size that counts 540,000 cells. A further refinement of 0.78125 mm was given to the power take-off (PTO) slot opening walls for all of the five mesh sizes (Mesh1–5). For all non-slip walls of the considered OWC, a first cell height equivalent to $y+\cong 1$ is used with a growth rate of 1.5 and 10 prism layers. Results in Fig. 2a show that the horizontal wave force (F_X) is almost identical for all considered mesh sizes, whereas the vertical force (F_Z) in Fig. 2b seems to be independent of the mesh size starting from Mesh3. Considering the computational time, Mesh3 is selected for the rest of the simulations performed in the present study.

2.3. CFD model validation

The considered CFD model was previously validated with experimental results for overall and detailed performance parameters of OWCs including chamber differential air pressure, chamber water level elevation, overall hydrodynamic efficiency and detailed flow fields (velocity and vorticity)

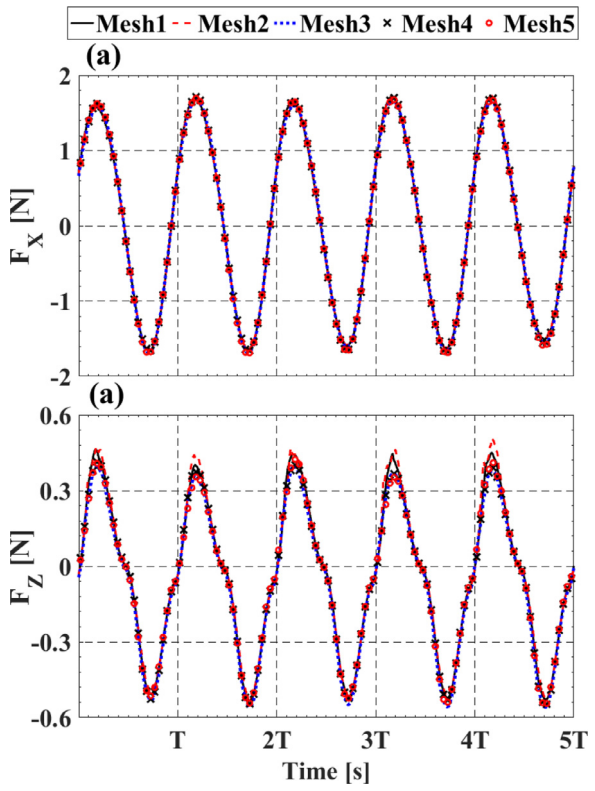

Fig. 2. Mesh convergence study. (a) Horizontal wave force (F_X) and (b) Vertical wave force (F_Z). $H = 50$ mm, $T = 1.2$ s and $e = 5.0$ mm.

[24,29]. Building on these validations, and considering the very limited reliable experimental data for hydrodynamic wave loads on OWCs in public literature under the action of nonlinear regular waves, the author decided to further validate the fully nonlinear CFD model utilized in this study against physical measurements including the reflection coefficient, transmission coefficient and wave loads acting on a 2D stationary-floating surface-piercing barge shown in Fig. 3 that is subjected to nonlinear regular waves [35]. The experimental results for this validation use a constant wave height $H = 70$ mm, water depth $h = L$, where L is the incident wavelength and a range of wave periods represented by a non-dimensional wavenumber (ζ) given by Eq. (1). The experimental results were also represented in non-dimensional forms for different parameters given in Eqs. (2)–(5) including: reflection coefficient (C_R), transmission coefficient (C_T), normalized horizontal force (F_X^*) and normalized vertical force (F_Z^*). The above-mentioned parameters are numerically calculated with the CFD model and compared against the experimental results conducted by Nojiri and Murayama [35] and others numerical results such as Tanizawa et al. [36]. Incident and reflected waves are resolved via utilizing three numerical wave probes (WPs) placed in front of the OWC at spacing as proposed by Mansard and Funke [37]. The spacing between wave probes were adjusted based on the incoming wavelength, so that the first WP is always located at a distance equal to one wavelength (L) from the OWC's front lip, the second WP at $0.9L$ and the third WP

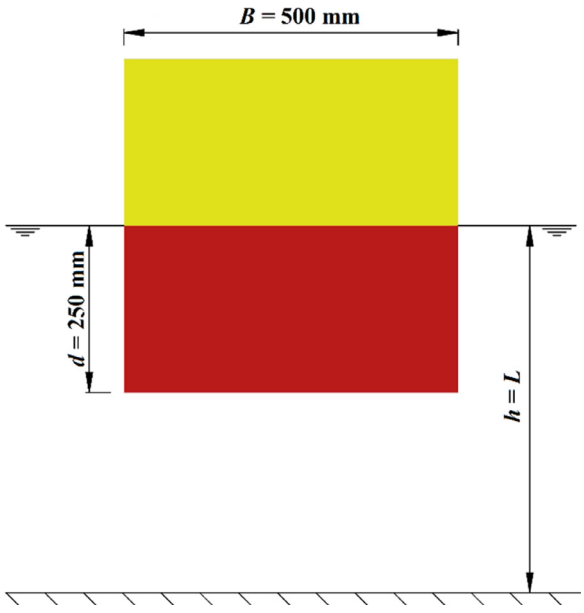

Fig. 3. Stationary-floating surface-piercing barge.

at $0.75L$, which is more that $0.2L$ as recommended by Goda and Suzuki [38] in case of regular wave tests. The transmitted wave height is monitored at a distance of about one wavelength behind the OWC's leeward lip. A mesh convergence study consisting of five mesh sizes ranging from 75,000 cells to 340,000 cells was also performed for this model (full results are not presented), and the selected mesh size was 12.5 mm (140,000 cells). The comparison results illustrated in Fig. 4 revealed that the present CFD model results are in good agreement with both experimental and others numerical results, which provides reasonable confidence in the capability of the utilized CFD model for accurately simulating the nonlinear waves interacting with a fixed bluff body such as a stationary-floating OWC.

$$\zeta = \frac{\omega^2 B}{2g} \tag{1}$$

where ω is the wave angular frequency, B is the barge length in the wave propagation direction and g is the gravitational acceleration.

$$C_R = \frac{H_R}{H} \tag{2}$$

$$C_T = \frac{H_T}{H} \tag{3}$$

where H, H_R and H_T are the incident, reflected and transmitted wave heights, respectively.

$$F_X{}^* = \frac{F_X}{\rho g W d A} \tag{4}$$

$$F_Z{}^* = \frac{F_Z}{\rho g W B A} \tag{5}$$

where F_X and F_Z are the measured horizontal and vertical wave loads, ρ is the water density (fresh water), d is the

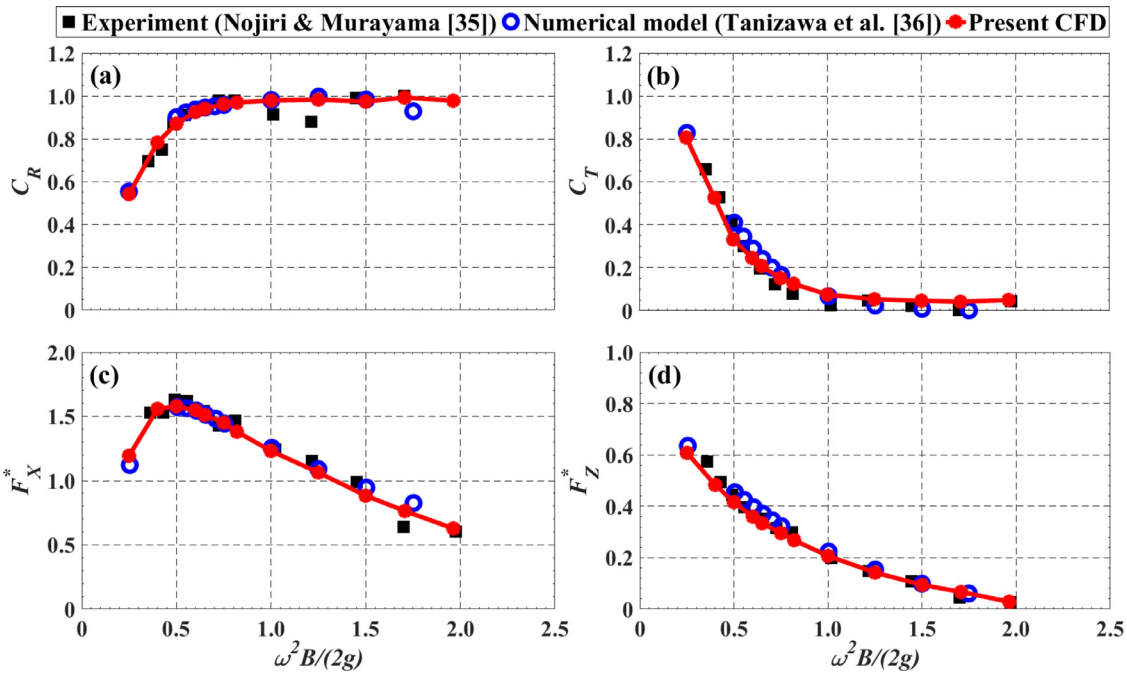

Fig. 4. CFD validation of regular wave interactions with a surface-piercing fixed barge. (a) reflection coefficient (C_R), (b) transmission coefficient (C_T), (c) normalized horizontal force (F_X^*) and (d) normalized vertical force (F_Z^*) versus nondimensional wavenumber $\zeta = \omega^2 B/2g$ under a regular wave height of $H = 70$ mm.

barge draft (250 mm), W is the barge breadth (not shown in Fig. 3) and A is the incident wave amplitude.

3. Wave loads on OWC

To investigate the hydrodynamic wave loads on an offshore-stationary OWC, the above well validated CFD model is utilized after replacing the surface-piercing barge in Fig. 3 with a 1:50 OWC model scale shown in Fig. 1b. The CFD model is then used to further study the wave–OWC interactions under fifteen wave periods (T) ranging from 0.8 to 2.2 s with 0.1 s increment that are represented by a dimensionless parameter Kb =1.8864–0.2494, where K is defined as $K=\omega^2/g$ and b is the chamber length in the wave propagation direction (see Fig. 1b), two wave heights (H) of 50 and 100 mm, eleven PTO damping simulated via different slot opening sizes (e)=1.5–9.0 mm and a constant water depth (h) of 1500 mm.

3.1. Wavelength effect

OWC interactions with a constant incoming wave height of 50 mm are studied in this section for the whole considered wave periods under three different PTO damping corresponding to a top slot size (e) of 6.0 mm (low damping), 3.0 mm (intermediate damping) and 1.5 mm (large damping). Starting with the horizontal wave force, considering that the surging force mainly results from the wave loads on the OWC's front and rear lips, the amplitude and phase shift between the two wave envelopes developed in front and behind the OWC structure are controlling the resultant force's amplitudes presented in Fig. 5c. The reflection and transmission coefficients, which are a function of the structural geometry and incoming waves can provide an indication of these envelopes. In addition, the radiated waves from the OWC chamber's internal free surface oscillation that depends on many factors such as wave characteristic and PTO damping may influence these wave envelopes. As seen in Fig. 5a, the reflection and transmission coefficients have fully opposite trends. Under low-frequency waves, the reflection and transmission coefficients are minimum and maximum, respectively. As the wavelength shortens, the reflection coefficient increases whereas transmission coefficient declines.

Considering the variations of these coefficients together with the trend of the horizontal wave force in Fig. 5c, it can be seen that under long waves, the amplitude and phase of forces acting on both lips are close to each other, which leads to a minimum resultant force. With increasing the wave frequency (Kb), the transmitted wave amplitude reduces; and therefore, the force amplitude on the aft wall decreases. On the other hand, increasing the reflection coefficient with Kb does not necessarily means enlarging the forces on the front wall. This is because the wave envelope in front of the OWC can be seen as a partial standing wave consisting of nodes and antinodes, and changing the phase between the incident, reflected and radiated waves will alter the position of these nodes and antinodes. However, considering that the resultant force increases with Kb, this explains the higher wave oscillations (antinodes) developed on or close to the front lip, which in turn improves the resultant force until getting its maximum at a certain Kb value. It is also interesting to see the horizontal force's peak occurs over a frequency (Kb) bandwidth

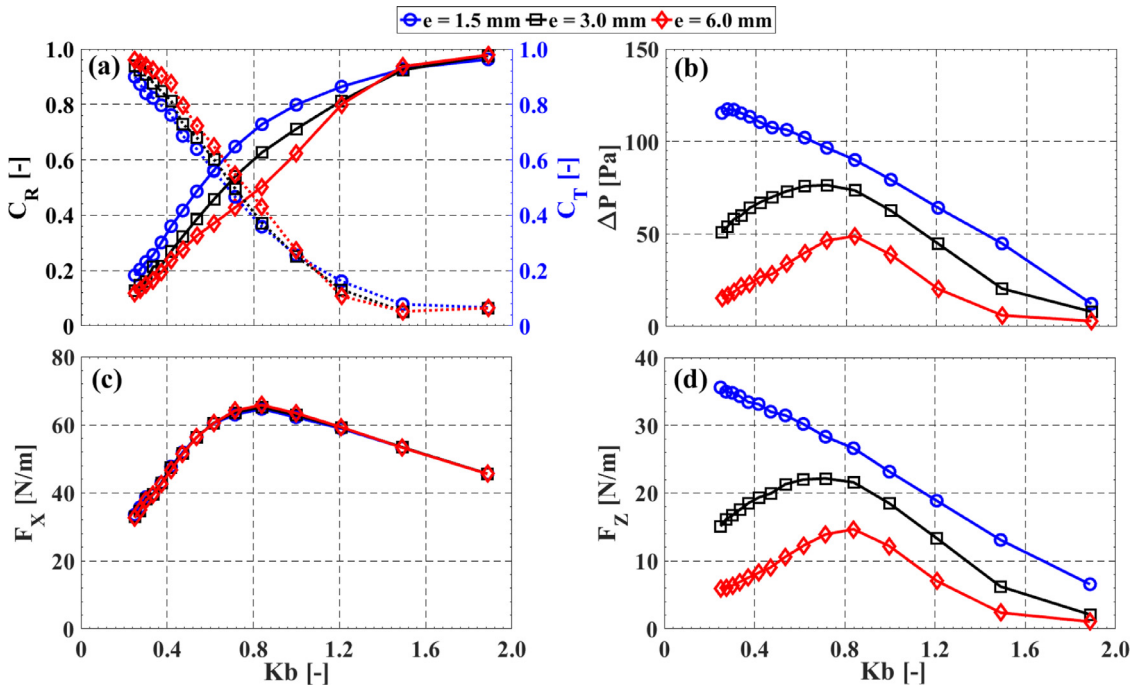

Fig. 5. OWC interactions with regular waves (H = 50 mm) versus nondimensional parameter (Kb) under different PTO slot opening size (e). (a) reflection (C_R) and transmission (C_T, dotted lines with markers) coefficients, (b) chamber's differential air pressure (ΔP), (c) horizontal wave force (F_X) and (d) vertical wave force (F_Z).

corresponds to the same frequency zone where both reflection and transmission coefficients are roughly equal, which is the same region of the maximum energy absorbed by the OWC structure [29]. Following this peak, while loads on the real lip keep decreasing due to the reduction in transmission coefficient with a further increase in Kb, forces on seaward wall seems to start declining, and the phase shift between both forces increases. Consequently, the total horizontal force declines. Additionally, under high–frequency waves, the chamber's free surface motion is no longer flat, and nonlinear effects as well as water sloshing increase, which are expected to influence the resultant force. For instance, the horizontal wave load per chamber's unit width (F_X) acting on the OWC and presented in Fig. 5c is seen to gradually increases from 33 N/m at Kb =0.2494 as the incoming wavelength decreases (i.e., Kb increases) till peaked with 66 N/m at a certain wavelength corresponding to a Kb = 0.8384. Following its maximum value, the horizontal force tends to linearly decrease with further shortening the wavelength up to 45 N/m at Kb = 1.886. Although, changing the PTO damping impacts the reflected and transmitted waves (Fig. 5a), it is observed that the predicted horizontal force is almost identical for the three simulated PTO damping, which again can be assigned to the change in phase shift on the measured forces considering that the applied damping significantly influences the chamber's free surface oscillation as well as the radiated waves. Further discussion is provided in Section 3.5.

Before discussing the hydrodynamic vertical wave loads, the chamber's differential air pressure is investigated. Results in Fig. 5b demonstrate that as the incoming wave becomes shorter (Kb increases), the differential air pressure amplitude (ΔP) increases before hitting its maxima at a given Kb value that represents the device natural frequency (resonance) or closer to that frequency [39]. Following the achieved peak value, the pressure amplitude progressively drops down. Changing the PTO damping affects the pressure amplitude and the device natural frequency, which in turn alters the Kb value at which the maximum pressure occurs. For instance, increasing the applied damping from e = 6.0 to 3.0 mm pushes the pressure peak from 49 Pa at Kb = 0.8384 to 76 Pa at a smaller Kb = 0.7144. This effect is also more obvious for the largest damping of e = 1.5 mm where the pressure peak of 117 Pa occurs almost under the longest wavelength (Kb = 0.2738). In addition to changing the resonance frequency (Kb value) and the corresponding peak pressure amplitude, increasing the PTO damping by reducing the slot opening (e) results in increasing the chamber pressure amplitude throughout the entire frequency range. Based on the differential air pressure results and the vertical wave loads presented in Fig. 5d, it is clear that the vertical wave force per chamber's unit width (F_Z) is following the same trend of the chamber's differential air pressure (ΔP) (Fig. 5b) for the whole tested frequencies (Kb) and PTO damping.

3.2. Wave height and PTO damping effects

Uncovering the impacts of increasing the incoming wave height two fold (i.e., H = 100 mm) on the predicted hydrodynamic loads are discussed in this section versus a 50 mm wave height over a series of PTO damping factors ($C = b/e$) and under three selected wave periods represented

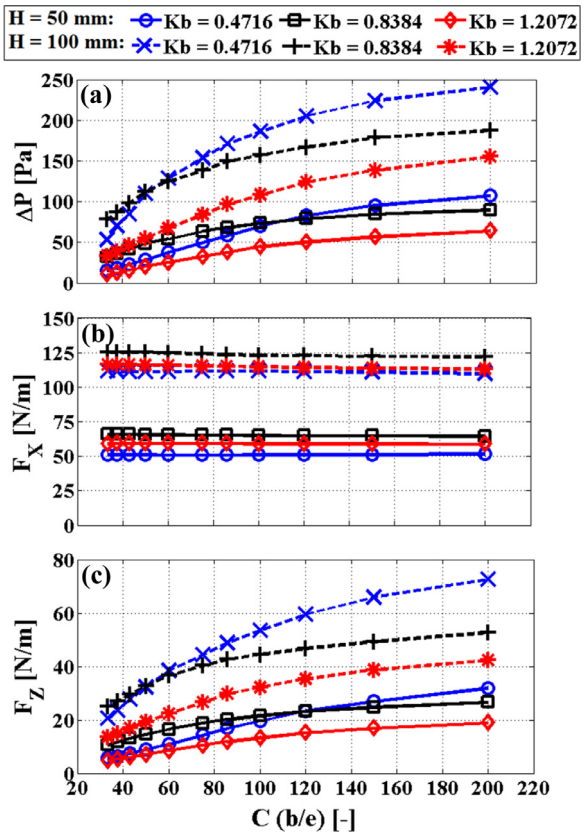

Fig. 6. Wave height impact on the OWC interactions with regular waves versus PTO damping factor (C) under different wavelengths (Kb). (a) chamber differential air pressure (ΔP), (b) horizontal force (F_X) and (c) vertical force (F_Z).

by $Kb = 0.4716$ (long wave, low steepness $H/L = 0.025$), 0.8384 (intermediate wavelength, $H/L = 0.044$) and 1.2072 (short wave, high-frequency and steepness of 0.064). Fig. 6a illustrates that air pressure amplitude (ΔP) increases with either increasing the PTO damping factor (C) or escalating the incident wave height for the three simulated wavelengths ($Kb = 0.4716$, 0.8384 and 1.2072). The higher wave frequency ($Kb = 1.2072$) provides the lower pressure amplitude over the 11 tested PTO damping and wave heights ($H = 50$ and 100 mm). The large PTO damping factors (C higher than 110) induce the higher pressure amplitudes when the OWC interacts with low frequency (long) waves ($Kb = 0.4716$) and height of 50 mm, whereas doubling the wave height shifts this damping factor limit ($C = 110$) to a lower value of $C = 50$, which widens and shortens the damping factor range that provides the higher pressure amplitudes for the low and intermediate wave frequencies, accordingly.

The horizontal wave force (F_X) shown in Fig. 6b provides that over the whole tested damping factors (C), the maximum force occurs at the intermediate wavelength, and changing the damping factor does not affect the predicted force (variation within + 1.07 % to − 1.70 % off the mean value). Conversely, doubling the wave height significantly magnifies the force amplitude by almost two times. Results in Fig. 6c illustrate that the influences the damping factor and wave height have

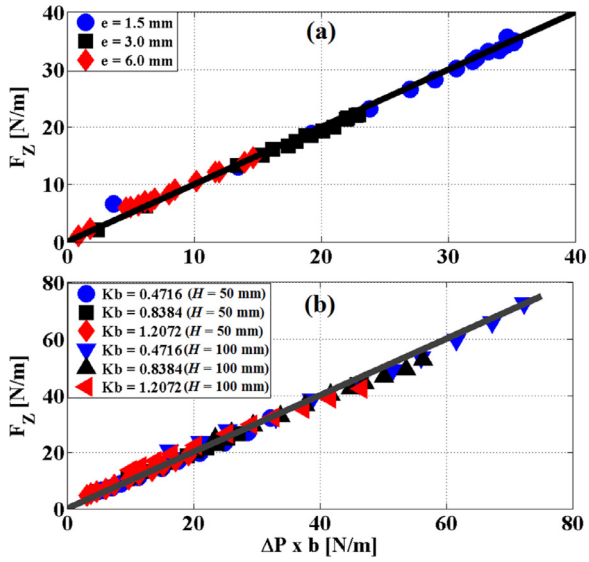

Fig. 7. Comparison between the hydrodynamic vertical wave force (F_Z) and the pneumatic force ($\Delta P\, x\, b$). (a) comparison for different wavelengths (Kb) and three damping (e) under a 50 mm wave height and (b) comparison for different wave heights ($H = 50$ and 100 mm) over different damping factors under three wavelengths (Kb).

on the vertical wave force (F_Z) are also similar to those on the chamber differential air pressure presented in Fig. 6a.

Considering the findings in Figs. 5 and 6, it seems that there is a good correlation between the chamber's differential air pressure (ΔP) and the hydrodynamic vertical force (F_Z). In order to discover this relation, Fig. 7 shows the hydrodynamic vertical wave force acting on the whole OWC structure (F_Z) in comparison with the pneumatic air (aerodynamic) force acting on the chamber's top plate that is defined as the product of the chamber's differential air pressure (ΔP) and the chamber's length (b). Fig. 7a demonstrates the forces resulting from Fig. 5b and d (i.e., the pneumatic and hydrodynamic vertical forces for the entire frequency range under three different damping of $e = 1.5$, 3.0 and 6.0 mm), while Fig. 7b compares the resulting pneumatic vertical forces (corresponding to air differential pressure amplitudes in Fig. 6a) and the hydrodynamic vertical forces (presented in Fig. 6c) over the whole studied 11 PTO damping factors (C) and two wave heights ($H = 50$ and 100 mm) for three wavelengths ($Kb = 0.4716$, 0.8384 and 1.2072). It is obvious from these results that the wave hydrodynamic vertical force is linearly proportional to the pneumatic differential air pressure force on OWC's top plate.

3.3. Horizontal versus vertical wave loads

The above discussed results show that the wave frequency (Kb) and damping factor (C) at which the maximum force occurs is different for the horizontal (F_X) and vertical (F_Z) wave forces. Also, the variation in each force is not synchronized with the each other. Accordingly, the ratio between these forces are studied in this section. Fig. 8 indicates that the horizontal force is always larger than the vertical force

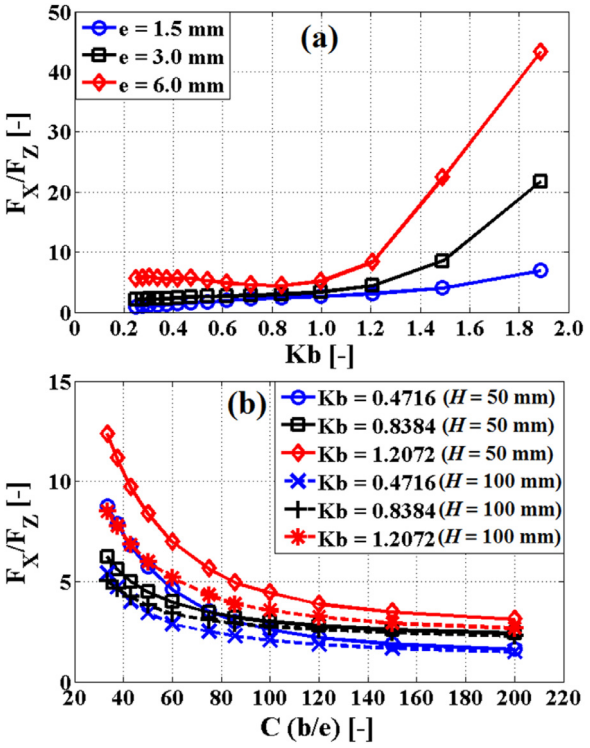

Fig. 8. Comparison between the horizontal (F_X) and vertical (F_Z) wave forces. (a) comparison for different wavelengths (Kb) and three PTO damping (e) under 50 mm wave height and (b) comparison for different wave heights (H = 50 and 100 mm) over different damping factors under three wavelengths (Kb).

for the whole tested wavelengths, damping factors and wave heights. The ratio between these forces (F_X/F_Z) is shown in Fig. 8a throughout the simulated wave frequencies for three PTO damping (e = 1.5, 3.0 and 6.0). The smaller damping (e = 6.0 mm) results in higher force ratios in comparison with the larger damping of e = 1.5 mm due to the smaller vertical forces induced by the larger damping (see Fig. 5d). Furthermore, as the wavelength decreases (Kb increases), the force ratio gradually increases from 1.0 at Kb = 0.2494 to 3.0 at Kb = 1.2072 and from 2.0 to 4.5 for e = 1.5 and 3.0 mm, respectively, whereas this ratio slightly declines for e = 6.0 mm from 5.5 at Kb = 0.2494 to 4.5 at Kb = 0.8384 (peak of F_X and F_Z in Fig. 5), before it also starts increasing. The increasing rate/slope of this ratio for the three damping values incredibly increases over the higher-frequency zone especially after Kb = 1.2072, which is more obvious for e = 3.0 and 6.0 mm. This can be assigned to the higher reduction rate in the vertical forces under higher frequencies (Fig. 5d) in comparison with the steady drop in the horizontal forces at high-frequency zone (Fig. 5c). For example, at the shortest (highest steep) wave of Kb = 1.886, the horizontal wave force (F_X) escalates up to 7.0, 22.0 and 43.0 times the vertical force (F_Z) under PTO damping e = 1.5, 3.0 and 6.0 mm, respectively.

At a given wavelength (Kb = 0.4716, 0.8384 or 1.2072), increasing the applied PTO damping factor from C = 33.33 (e = 9.0 mm) to 200 (e = 1.5 mm) results in reducing the force ratio as shown in Fig. 8b, which is a consequence of increasing the vertical forces with damping, whereas no effects on the horizontal forces (Fig. 6b and c). This reduction is more pronounced up to C = 120 where the force ratio drops from about 8.8, 6.2 and 12.4 at C = 33.22 for Kb = 0.4716, 0.8384 and 1.2072, respectively to almost 2.2, 2.8 and 3.9. Following this threshold (C = 120), the damping effect becomes little, which can be seen in the minor further reduction in the force ratio to 1.6, 2.4 and 3.1. Although increasing the wave height leads to increasing both the horizontal (Fig. 6b) and vertical (Fig. 6c) wave forces, the ratio between these forces (F_X/F_Z) is seen in Fig. 8b to decrease as the wave height increases to 100 mm, especially under small PTO damping, which in turn indicates that the vertical force is more sensitive to increasing the wave height than the horizontal force. For instance, at H = 100 mm, the force ratio drops to an average of 0.7, 0.9 and 0.75 times the ratios at H = 50 mm for Kb = 0.4716, 0.8384 and 1.2072, respectively that provides less effect on the intermediate wavelength. Having the correlation between the aerodynamic and hydrodynamic vertical wave forces (Fig. 7) together with the relation between the vertical and horizontal forces (Fig. 8), provides a possibility of utilizing the chamber's differential air pressure not only for estimating the device energy extraction efficiency, but also for predicting the loads acting on the device.

3.4. Nonlinear wave forces effect

The environmental conditions tested in this study provides a wide range of wave steepness 0.0075 ≤ H/L ≤ 0.064. Within this steepness range, the nonlinear effects change; therefore, its importance is discussed in this section. For each of the horizontal and vertical wave forces, time series data of five wave cycles are carefully selected. Fast Fourier Transform (FFT) is then used to resolve the energy contents in each frequency (fundamental wave frequency and its higher harmonics up to 3nd harmonic). Fig. 9 compares the contribution of the higher harmonics (2nd and 3rd) to the forces acting on the OWC as a percentage of the total force where E_X and E_Z represent the total energy content in the predicted horizontal and vertical force, accordingly, and the subscripts 2 and 3 refer to the energy concentrated in the and 2nd and 3rd harmonics, respectively. Fig. 9a shows that up to a Kb = 1.2072, the higher harmonics in the vertical force contribute up to about 10% of the total predicted vertical force, and this effect is almost the same for the three PTO damping of e = 6.0, 3.0 and 1.5 mm with only a slight increase for e = 6.0 mm at low frequency waves. Afterwards the Kb of 1.2072, incoming waves become more steep and nonlinear effects are more pronounced and progressively increases up to 24, 20 and 16% for e = 6.0, 3.0 and 1.5 mm, accordingly. In contrast, nonlinear effects are less than 5% for the horizontal wave force as given in Fig. 9c.

Impact of increasing the wave height to 100 mm and changing the PTO damping factor on the higher harmonics' contribution to the predicted vertical and horizontal forces are illustrated in Fig. 9b and d, respectively. Fig. 9b shows

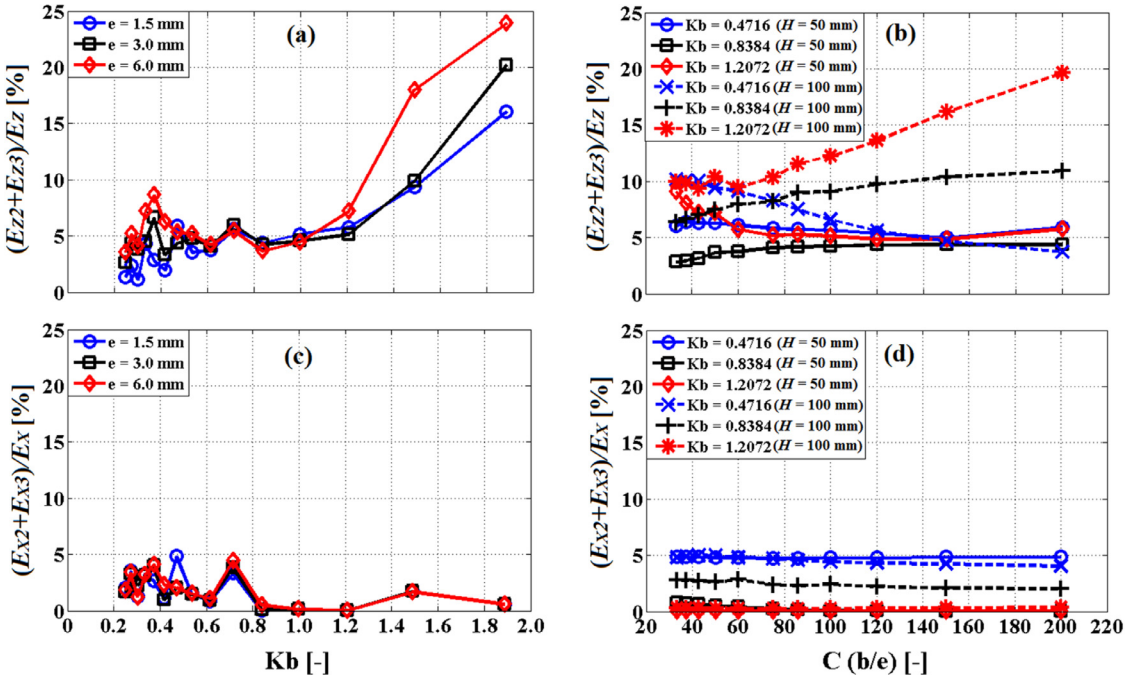

Fig. 9. Higher harmonics impacts on the predicted forces. (a and c) impacts of different wavelengths (Kb) and three PTO damping (e) under 50 mm wave height, (b and d) impacts of different PTO damping factors (C) and wave heights H = 50 and 100 mm for three wavelengths (Kb).

that as the damping factor (C) increases, nonlinear effects vary between 3.0 and 9.0% by either increasing from 3.0% at C = 33.33 to 4.5% at C = 200 for Kb = 0.8384 or decreasing from 9.0% to 6.0% for the shorter wavelength of Kb = 1.2072, where a slight variation of 5–6% is observed for the low frequency wave of Kb = 0.4716. Furthermore, after a damping factor (C) = 120, there is a little difference between the three tested wavelengths (Kb) that show almost a flat trend with a mean values of 5%. On the other side, increasing the wave height arises the nonlinear effects on the vertical wave forces (Fig. 9b), and these effects develop as the damping factor (C) escalates except for the longer waves where increasing the damping results in lesser nonlinear effects. For instance, under a short wavelength of Kb = 1.2072, nonlinear effects increase from 9% for H = 50 mm to 10% for H = 100 mm at C = 33.33 and from 6% to 19% at C = 200 for H = 50 mm and 100 mm, accordingly, while these effects are almost doubled throughout the whole damping range for the intermediate wavelength of Kb = 0.8384. For the horizontal (surge) force, nonlinear higher harmonics effects are seen to be insensitive to the damping factor. Also, increasing the wave height shows a little impact on the nonlinear contribution to the surging force, especially for the lower (Kb = 0.4716) and higher (Kb = 1.2072) wave steepness. However, for the intermediate wavelength (Kb = 0.8384), doubling the wave height escalates the nonlinear effect from only 0.35% to about 2.5%.

Time series data and corresponding FFT results are shown in Fig. 10 for a wavelength of Kb = 1.2072 under different wave heights and PTO damping. Fig. 10a and b confirm the results shown in Fig. 9d where a damping of e = 1.5 and 6.0 mm under wave heights of H = 50 and 100 mm result in a negligible nonlinear effect on the surging force with almost symmetric crest/trough time series data in Fig. 10a; accordingly, all energy (S_X) is concentrated in the fundamental incoming wave frequency of 1.0 Hz as shown in Fig. 10b. On the other side, nonlinear effects on the vertical forces are more obvious for a damping e = 1.5 mm and a wave height of 100 mm (see Fig. 9b) that is shown by the larger negative force (trough) in comparison with the positive value (crest) in Fig. 10c. This nonlinearity is represented by a second energy spike (S_Z) at the 2nd harmonic of 2.0 Hz in Fig. 10d, and represents about 17.5% of the total energy, while other analyzed conditions show only one peak value at the wave frequency with small/negligible second spike at the 2nd harmonic.

Similar to analyzing results for a short wavelength of Kb = 1.2072, time series data and FFT results for an intermediate wavelength of Kb = 0.8384 are shown in Fig. 11 with a damping e = 1.5 and 5.0 mm under wave heights of H = 50 and 100 mm. Fig. 11a and b illustrate the minor nonlinear effects on the horizontal surging force. Conversely, Fig. 11c and d highlight the nonlinear impacts on the predicted vertical force that are more clear under the larger wave height and PTO damping (H = 100 mm and e = 1.5 mm) with the second peak in FFT results representing about 9% of the total energy content in the predicted force.

3.5. 3D and PTO modeling effects

The above-discussed results are limited to 2D flow assumptions. In order to investigate the impacts the 3D modeling may have on the predicted hydrodynamic loads, the developed 2D CFD model in Section 2 is extended to 3D domain with boundary conditions as illustrated in Fig. 12a. Consid-

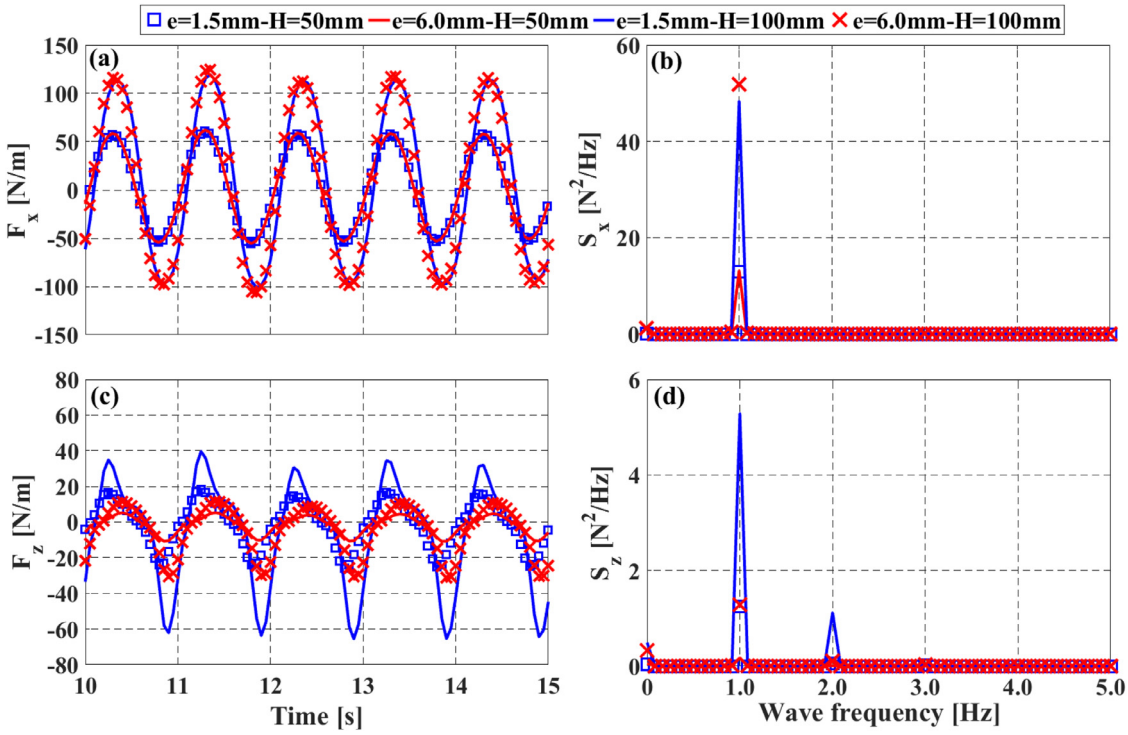

Fig. 10. Time series and FFT results of a damping $e = 1.5$ and 6.0 mm and a wave height $H = 50$ and 100 mm under a constant wavelength $Kb = 1.2072$. (a) horizontal force time series, (b) horizontal force FFT results, (c) vertical force time series, (d) vertical force FFT results.

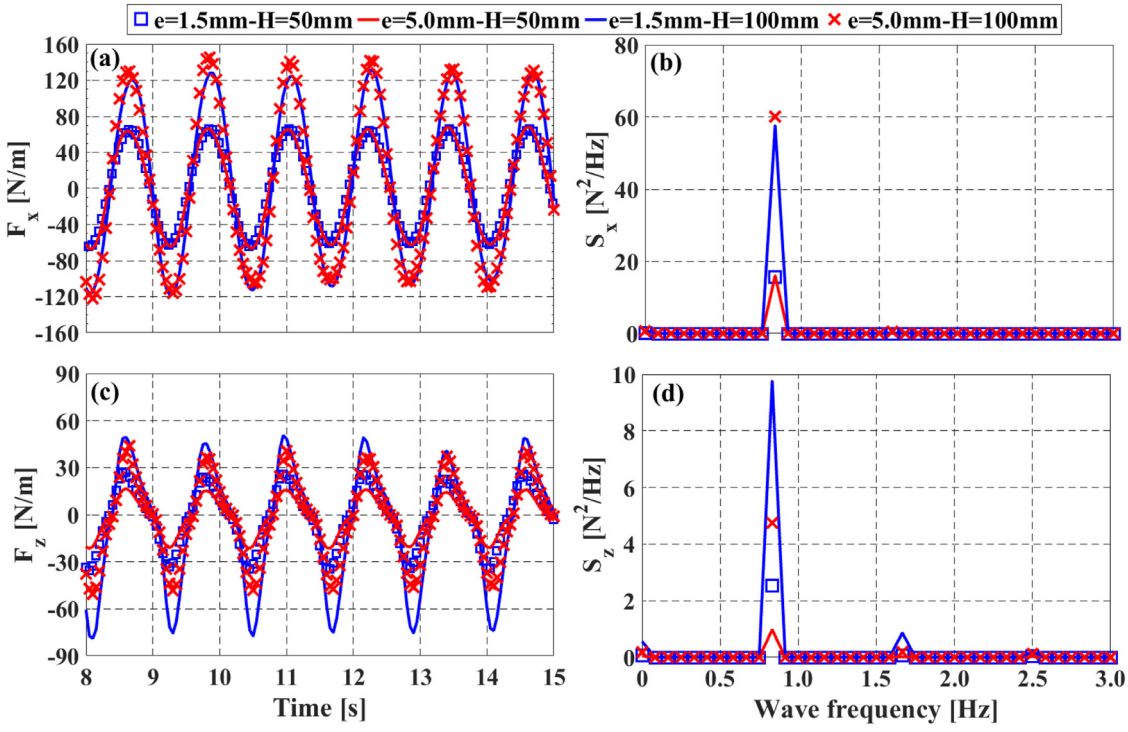

Fig. 11. Time series and FFT results of a damping $e = 1.5$ and 5.0 mm and a wave height $H = 50$ and 100 mm under a constant wavelength $Kb = 0.8384$. (a) horizontal force time series, (b) horizontal force FFT results, (c) vertical force time series, (d) vertical force FFT results.

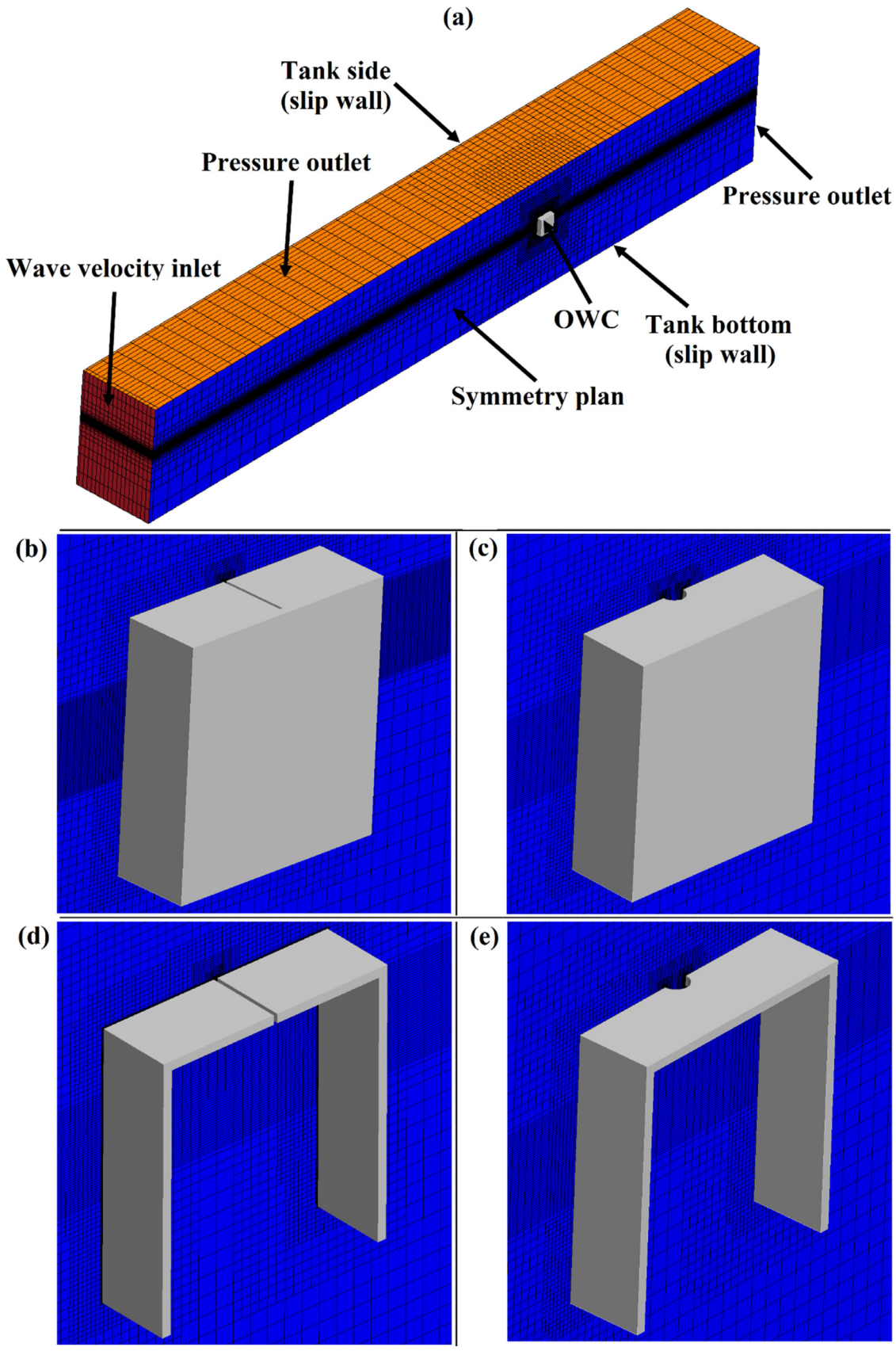

Fig. 12. 3D computational fluid domain. (a) Computational domain with mesh and boundary conditions, (b) 3D OWC with slot opening, (c) 3D OWC with orifice plate, (d) OWC with slot opening for flume tank and (e) OWC with orifice plate for flume tank.

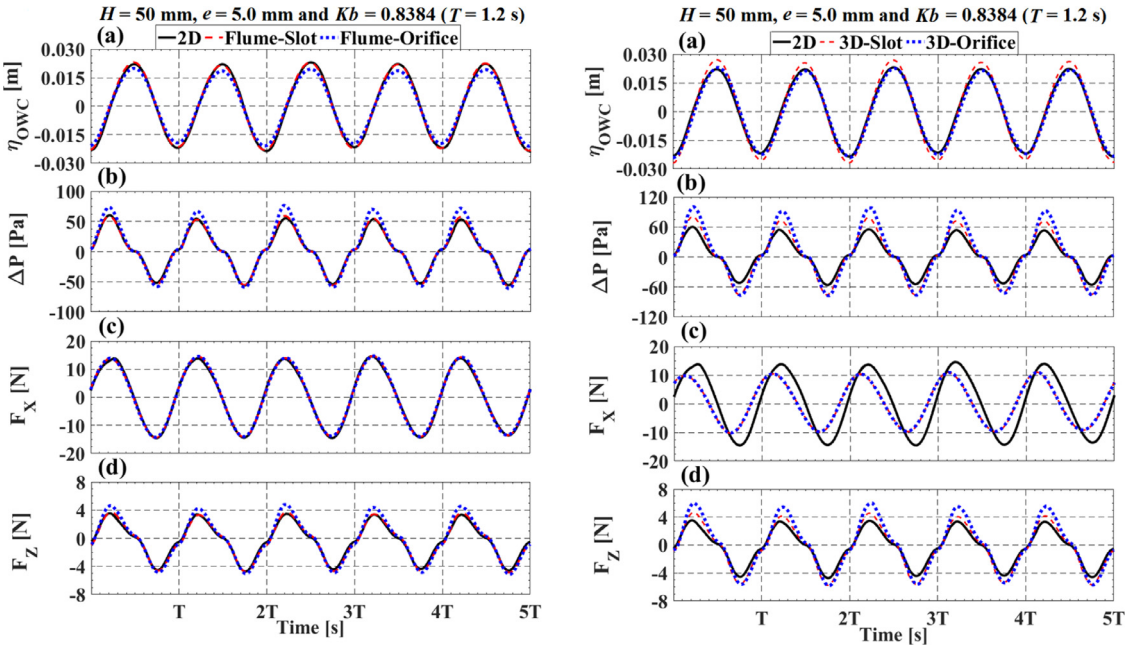

Fig. 13. 3D and PTO modeling effects on: (a) chamber's free surface oscillation (η_{OWC}), (b) chamber's differential air pressure (ΔP), (c) horizontal wave force (F_X) and (d) vertical wave force (F_Z). H = 50 mm, e = 5.0 mm and Kb = 0.8384 (T = 1.2 s).

ering that 3D modeling is time consuming, an intermediate stage between 2D and 3D modeling is investigated by testing the OWC in a numerical tank flume of breadth equal to the OWC's pneumatic chamber width of 100 mm with a symmetry plan. Results of this wave flume are compared with those from a fully 3D tank with breadth of 1750 mm (model's width is about 0.06 of the tank's breadth) that is enough to ignore the sidewall effects [40]. In addition, simulating the PTO damping via a slot opening restricts the flow to 2D; accordingly, a comparison between using a slot opening (2D) and an orifice plate (3D) with the same opening ratio (the ratio between the PTO opening and the chamber's water plan area) is also included. All model's configurations are illustrated in Fig. 12b to e. To investigate all these parameters, testing conditions were limited to only one wave height of H = 50 mm, a slot opening e = 5.0 mm and three wave periods of T = 1.0 s (Kb = 1.2072), 1.2 s (Kb = 0.8384) and 1.6 s (Kb = 0.4716). Measurements include OWC's free surface oscillations (η_{OWC} that is based on an average of 25 numerical wave probes placed inside the pneumatic chamber), chamber's differential air pressure (average of 10 monitoring points) and the horizontal and vertical wave loads.

Starting with tank flume modeling and orifice plate effects on the predicted loads under a wave frequency of Kb = 0.8384, which results in the maximum loads under the considered PTO damping (e = 5.0 mm or C = 60, see Fig. 6), results in Fig. 13left illustrate that testing in tank flumes with PTO modeled with a slot opening provides almost the same results as 2D modeling for all measured parameters, except a slight increase of 4% in the vertical force. On the other hand, using an orifice plate (with a radius of 17.84 mm) instead of the slot opening induces higher air pressure (Fig. 13left-b) that in agreement with the experimental observations by He and Huang [41], which in turn reduces the chamber's free surface oscillation amplitude (Fig. 13left-a) and enlarges the hydrodynamic vertical forces (Fig. 13left-d) by 14.5% due to its coupling with the pneumatic force as discussed in Section 3.2. It is however, as discussed in Section 3.2, the horizontal forces (Fig. 13left-c) are independent of the applied damping that explains the identical results from PTO modeling with either a slot opening or an orifice plate.

In 3D modeling, not only wave scattering is considered, but also, removing the 2D flow restriction allows the water column to evacuate the chamber more easily, which in turn escalates the chamber's free surface oscillation amplitude as seen in Fig. 13right-a for OWC with 3D slot opening. In addition, for OWC with an orifice plate, the free surface oscillation amplitude increased in comparison with tank flume' results (Fig. 13left-a), but the oscillation is lower that the case with slot opening due to the higher damping induced by the orifice plate. This increase in the oscillation amplitude under a given wave period and PTO damping increases the oscillation rate (slope), which in turn escalates the air pressure amplitude (Fig. 13right-b) as well as the airflow rate through the PTO [29]. Similar to the tank flume, using the orifice plate improves the air pressure in comparison with the slot opening, and this effect is more obvious during the exhalation (pressurizing) stage. Having explained the increase in air pressure, it is expected that also the vertical wave forces in 3D modeling (Fig. 13right-d) are higher than those from flume tanks, and this increase found to be almost 20% for 3D with slot opening versus flume with slot opening, 20% for 3D with orifice plate versus flume with orifice plate and about 43% for 3D with orifice plate in comparison with 2D

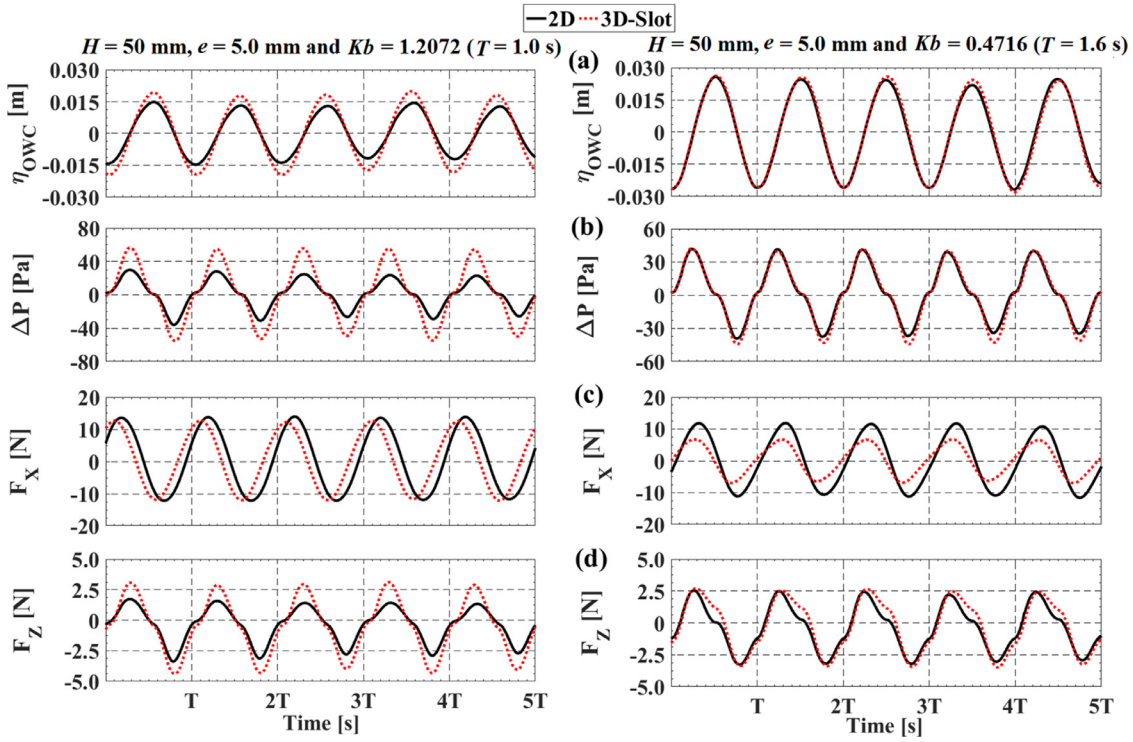

Fig. 14. 3D effects on: (a) chamber's free surface oscillation (η_{OWC}), (b) chamber's differential air pressure (ΔP), (c) horizontal wave force (F_X) and (d) vertical wave force (F_Z). H = 50 mm, e = 5.0 mm, Kb = 1.2072 (left) and Kb = 0.4716 (right).

modeling. Conversely, the horizontal wave loads in 3D modeling shown in Fig. 11right-c are lower that tank flume (or 2D) measurements. Further explanation regarding these reductions in surging forces is given later in this section.

Similar to the observations of 3D effects on the maximum measured forces under a wavelength of Kb = 0.8384, results for additional wave frequencies of Kb = 1.2072 (Fig. 14left) and Kb =0.4716 (Fig. 14right) revealed the same impacts of 3D modeling. Additionally, these results illustrate that 3D modeling leads to a massive reduction and increase in the horizontal and vertical wave loads as the wavelength increases and decreases, respectively. For example, the reduction in horizontal loads (F_X) increases from 5% at Kb = 1.2072 (Fig. 14left-c) to 29% at Kb = 0.8384 (Fig. 13right-c) and then to 41% at Kb = 0.4716 (Fig. 14right-c). On the other hand, 3D simulations results in about 60% increase in the vertical wave force (F_Z) at Kb = 1.2072 (Fig. 14left-d) in comparison with 25% at Kb = 0.8384 (Fig. 13right-d, slot opening) and 7.5% at Kb = 0.4716 (Fig. 14right-d). Figs. 13 and 14 also highlight that 3D modeling not only affect the horizontal force amplitudes, but also, the frequency of the maximum force changes. For instance, the peak force was found at Kb = 0.8384 (Fig. 5c and time series data in Fig. 13c) in 2D modeling, but this peak seems to be shifted to a higher frequency of Kb = 1.2072 in 3D modeling (Fig. 14left-c).

As discussed in Section 3.1 the wave profile before and after the OWC is quite important for explaining the changes in the horizontal forces. For instance, results in Fig. 15 shows a comparison between 2D and 3D wave elevations for Kb = 0.8384 at four points along the tank on the symmetry plan (η_1–η_3 are placed before OWC and η_4 is located behind OWC). Coordinates of these points are similar to the wave probes' locations described in Section 2.3. Results illustrate that 3D modeling allows most of the incoming waves

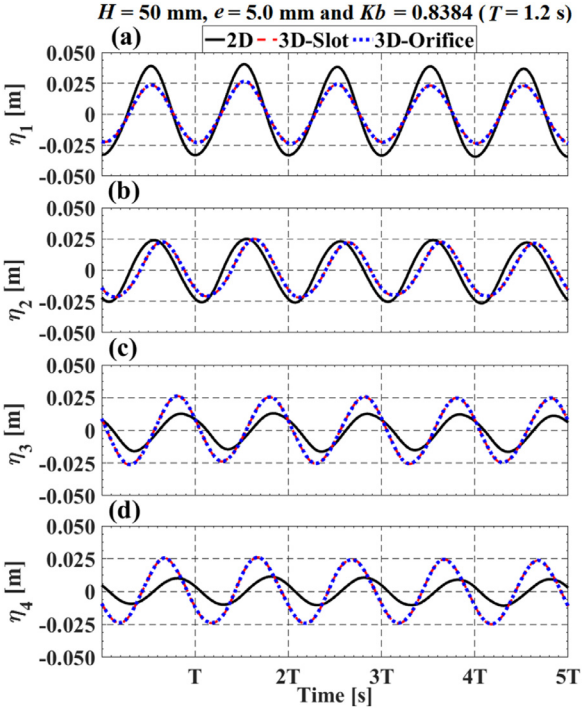

Fig. 15. 3D and PTO modeling effects on the wave envelope before and after OWC. H = 50 mm, e = 5.0 mm and Kb = 0.8384 (T = 1.2 s).

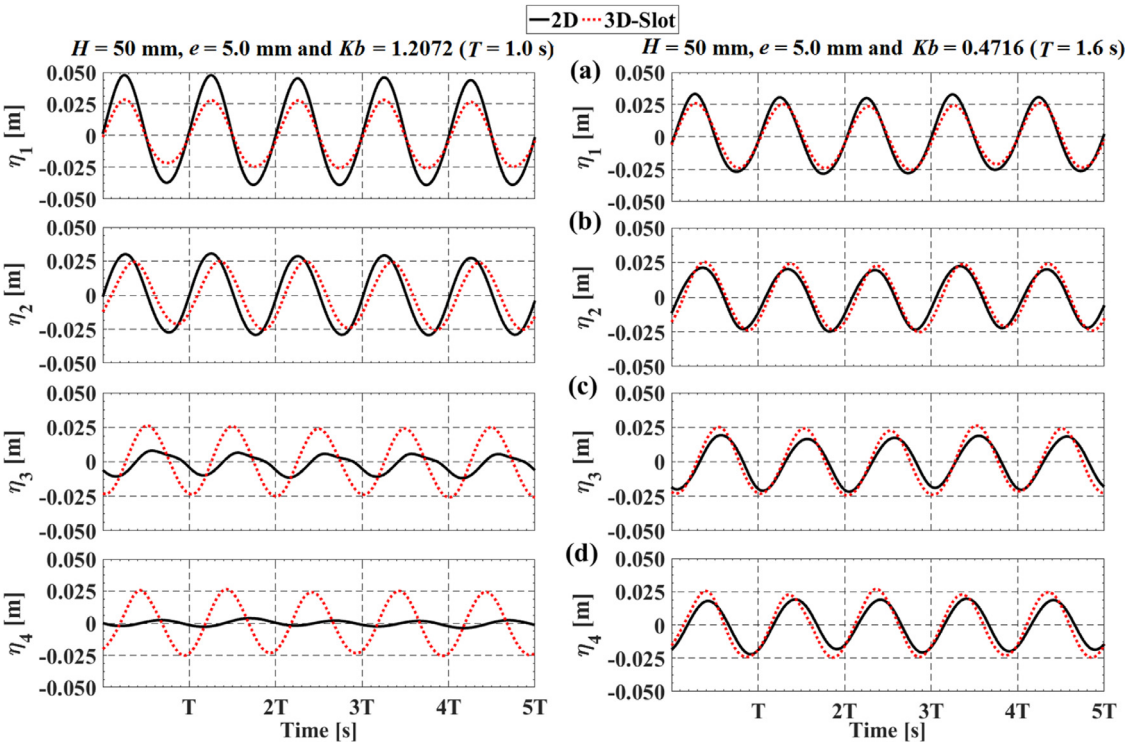

Fig. 16. 3D effects on the wave envelope before and after OWC. $H = 50$ mm, $e = 5.0$ mm, $Kb = 1.2702$ (left) and $Kb = 0.4716$ (right).

to be transmitted on the OWC's leeside, which can be seen in the consistency in the monitored wave amplitudes along the four points. Also, there is no visible impact of using an orifice plate rather than a slot opening. Furthermore, as reflection and transmission coefficients with 2D modeling are maximum and minimum respectively under short waves, it is expected that discrepancy with 3D modeling become more and less pronounced at high ($Kb = 1.2072$) and low ($Kb = 0.4716$) frequency waves as shown in Fig. 16left and right, respectively. These differences explain the overall reductions in the horizontal forces predicted with 3D modeling in comparison with 2D flow assumptions. However, to further clarify the escalation of these reductions with increasing the wavelength, the wave elevation is monitored and presented in Fig. 17 at two points closer to the OWC structure on each side: one at 50 mm in front of the OWC's seaward wall (Before OWC) and another one 50 mm behind the leeside (After OWC). It is clear that as the wavelength increases (Kb decreases), the wave amplitude after OWC with respect to the wave amplitude before OWC increases, while the phase shift between each wave trend diminishes (phase shift is $0.34T$ at $Kb = 1.2072$, $0.26T$ at $Kb = 0.8384$ and $0.16T$ at $Kb = 0.4716$). As a result, a large reduction in surging forces is more obvious under long waves in comparison with 2D results.

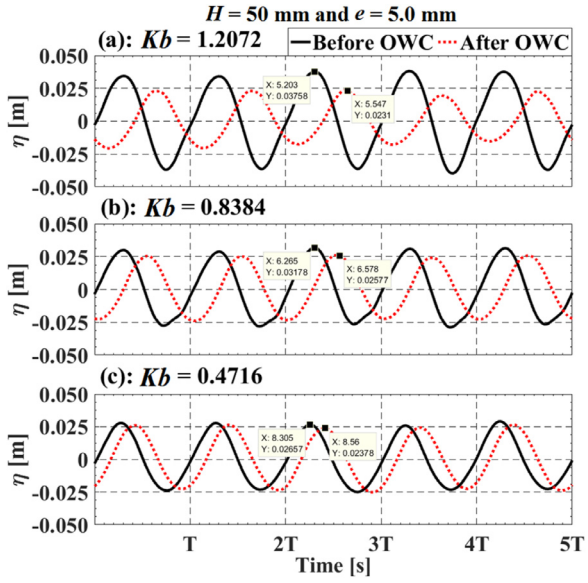

Fig. 17. 3D effects on the wave elevation at 50 mm before and after OWC. (a): $Kb = 1.2702$, (b): $Kb = 0.8384$ and (c): $Kb = 0.4716$. $H = 50$ mm, $e = 5.0$ mm.

4. Conclusions

2D and 3D CFD models based on RANS–VOF are implemented in this paper in order to study the hydrodynamic wave loads on an offshore-stationary OWC over a wide range of wave periods, wave heights and pneumatic damping. The model is validated in good agreement against nonlinear regular wave interactions with a surface-piercing fixed barge. From the investigations carried out of total 108 numerical tests, the following conclusions are drawn:

- The hydrodynamic horizontal wave load is independent of the applied PTO damping even with increasing the incoming wave height.
- Increasing the wave height by two times leads to almost doubling the surging wave force.
- The maximum horizontal force occurs at frequency bandwidth where reflection and transmission coefficients are almost the same.
- The predicted vertical hydrodynamic load is following the same variation of the chamber's differential air pressure with a peak value almost at the OWC natural frequency.
- The hydrodynamic vertical force is linearly proportional to the pneumatic air force acting on the chamber's top plate.
- Regardless of the incoming wave frequency, height and PTO damping, the hydrodynamic horizontal force is always larger than the vertical force.
- The ratio between the horizontal and vertical wave forces is higher for high frequency waves, smaller wave height and lower PTO damping.
- Nonlinear effects are more pronounced in the vertical force than the horizontal one.
- Nonlinearity contributes to about less than 5% of the total surging force energy, whereas this contribution can extend to 24% for the vertical force under high frequency waves.
- Testing offshore OWCs in tank flumes provides the same results as 2D modeling.
- Simulating the PTO damping with an orifice plate of the same opening ratio of a slot opening leads to high chamber's differential air pressure and in turn larger vertical wave force, whereas no impact on the horizontal force was found.
- 3D modeling results in reducing the horizontal wave forces, and this impact increases with increasing the wavelength.
- The maximum horizontal force in 3D modeling is shifted to a higher frequency in comparison with 2D modeling.
- 3D modeling leads to higher chamber's free surface oscillations, larger air pressure, and accordingly escalates the pneumatic and hydrodynamic vertical wave forces. These effects become more noticeable as the wavelength shortens.

Although the present work provided an overview on the hydrodynamic wave loads that an offshore OWC may experience during operational conditions (small waves), results were validated against two-dimensional model. Accordingly, as a continuation of this research, experiments will be performed to validate the numerical results not only for the 3D effects, but also under extreme environmental conditions representing survival events. Additionally, air compressibility may impact the predicted wave loads on the device, especially for large-scale prototypes [42], thus scaling effects with both incompressible and compressible airflow will be investigated.

Acknowledgement

The author is thankful to Associate Professor Gregor MacFarlane, Australian Maritime College, University of Tasmania, Australia for the preliminary review of this article. In addition, the author thanks the National Centre for Maritime Engineering and Hydrodynamics, Australian Maritime College, University of Tasmania, Australia for the financial support of his PhD.

References

[1] D. Evans, IMA J. Appl. Math. 22 (1978) 423–433.
[2] A.d.O. Falcão, A. Sarmento, in: 15th International Congress of Theoretical and Applied Mechanics, Toronto, Canada, 1980.
[3] D. Evans, J Fluid Mech. 114 (1982) 481–499.
[4] J. Falnes, P. McIver, Appl. Ocean Res. 7 (1985) 225–234.
[5] A.J. Sarmento, A.d.O. Falcão, J. Fluid Mech. 150 (1985) 467–485.
[6] A. Sarmento, Exp. Fluids 12 (1992) 286–292.
[7] M.T. Morris-Thomas, R.J. Irvin, K.P. Thiagarajan, J. Offshore Mech. Arct. Eng. 129 (2007) 273–278.
[8] D.-Z. Ning, R.-Q. Wang, Q.-P. Zou, B. Teng, Appl. Energy 168 (2016) 636–648.
[9] A. Brito-Melo, T. Hofmann, A. Sarmento, A. Clément, G. Delhommeau, Int. J. Offshore Polar Eng. 11 (2001).
[10] Y. Delauré, A. Lewis, Ocean Eng. 30 (2003) 309–330.
[11] C. Josset, A. Clément, Renew. Energy 32 (2007) 1379–1402.
[12] M. Lopes, P. Ricci, L. Gato, A.d.O. Falcão, in: Proceedings of the 7th European Wave and Tidal Energy Conference, Porto, Portugal, 2007.
[13] R. Sykes, A. Lewis, G. Thomas, in: Proceedings of the 7th European Wave and Tidal Energy Conference, Porto (Portugal), 2007.
[14] R. Sykes, A. Lewis, G. Thomas, in: Proceedings of the 8th European Wave & Tidal Energy Conference, Uppsala, Sweden, 2009.
[15] R. Gomes, J. Henriques, L. Gato, A. Falcao, Renew. Energy 44 (2012) 328–339.
[16] Y. Zhang, Q.-P. Zou, D. Greaves, Renew. Energy 41 (2012) 159–170.
[17] P.R. Teixeira, D.P. Davyt, E. Didier, R. Ramalhais, Energy 61 (2013) 513–530.
[18] I. López, B. Pereiras, F. Castro, G. Iglesias, Appl. Energy 127 (2014) 105–114.
[19] A. Kamath, H. Bihs, Ø.A. Arntsen, Int. J. Mar. Energy 10 (2015) 1–16.
[20] A. Kamath, H. Bihs, Ø.A. Arntsen, Ocean Eng. 102 (2015) 40–50.
[21] Y. Luo, J.-R. Nader, P. Cooper, S.-P. Zhu, Renew. Energy 64 (2014) 255–265.
[22] M. Anbarsooz, A. Faramarzi, A. Ghasemi, in: POWER & ENERGY Conference & Exhibition, Charlotte, USA, 2016.
[23] U. Şentürk, A. Özdamar, Prog. Comput. Fluid Dyn. Int. J. 13 (2013) 120–129.
[24] A. Elhanafi, A. Fleming, G. MacFarlane, Z. Leong, Energy (2016) (in press, doi:10.1016/j.energy.2016.09.118).
[25] A. Iturrioz, R. Guanche, J. Armesto, M. Alves, C. Vidal, I. Losada, Ocean Eng. 76 (2014) 65–74.
[26] A. Iturrioz, R. Guanche, J. Lara, C. Vidal, I. Losada, Ocean Eng. 107 (2015) 222–236.
[27] I. Crema, I. Simonetti, L. Cappietti, H. Oumeraci, in: 11 th European Wave and Tidal Energy Conference (EWTEC), Nantes, France, 2015.
[28] I. Simonetti, L. Cappietti, H. El Safti, H. Oumeraci, in: ASME 2015 34th International Conference on Ocean, Offshore and Arctic Engineering, Volume 9: Ocean Renewable Energy, American Society of Mechanical Engineers, St. John's, Newfoundland, Canada, 2015 (OMAE2015-42056).
[29] A. Elhanafi, A. Fleming, G. MacFarlane, Z. Leong, Int. J. Nav. Archit. Ocean Eng. (IJNAOE) (2016) (in press, doi:10.1016/j.ijnaoe.2016.08.002).
[30] A. Elhanafi, A. Fleming, G. MacFarlane, Z. Leong, Renew. Energy (2016) (provisionally accepted).

[31] V.S. Jayakumar, Wave force on oscillating water column type wave energy caisson: an experiment study, PhD Thesis in: Department of Ocean Engineering, Indian Institute of Technology Madras, India, 1994.
[32] S.J. Ashlin, S. Sannasiraj, V. Sundar, Procedia Eng. 116 (2015) 1019–1026.
[33] C.W. Hirt, B.D. Nichols, J. Comput. Phys. 39 (1981) 201–225.
[34] A. Elhanafi, A. Fleming, Z. Leong, G. Macfarlane, Prog. Comput. Fluid Dyn. (2016) (in press).
[35] N. Nojiri, K. Murayama, in: Transactions of the West-Japan Society of Naval Architects, 131, 1975, p. 152.
[36] K. Tanizawa, M. Minami, S. Naito, in: The Ninth International Offshore and Polar Engineering Conference, International Society of Offshore and Polar Engineers, 1999.
[37] E.P. Mansard, E. Funke, Coast. Eng. Proc. 1 (1980).
[38] Y. Goda, T. Suzuki, Coast. Eng. Proc. 1 (1976).
[39] D.-Z. Ning, J. Shi, Q.-P. Zou, B. Teng, Energy 83 (2015) 177–188.
[40] S.K. Chakrabarti, Offshore structure modeling, World Scientific Publishing, Singapore, 1994.
[41] F. He, Z. Huang, Ocean Eng. 88 (2014) 618–626.
[42] A.F. Falcão, J.C. Henriques, Int. J. Mar. Energy 6 (2014) 18–34.